Sea target detection using the GNSS reflection signals

Zhenyu He[1] · Wu Chen[2] · Yang Yang[2] · Mingwei Shen[1]

Zhenyu He

20220261@hhu.edu.cn

Wu Chen

wu.chen@polyu.edu.hk

Yang Yang

yyang.yang@connect.polyu.hk

Mingwei Shen (**Corresponding author**)

smw_nuaa@hotmail.com

1 School of Computer and Information, Hohai University, Nanjing 211100, PR China

2 Department of Land Surveying and Geo-Informatics, The Hong Kong Polytechnic University, Hong Kong 999077, PR China

Abstract Global navigation satellite system (GNSS) reflection signal to form a passive radar system for sea target detection has attracted attention in recent years. Low signal power on the earth's surface is the main bottleneck of this passive radar system. Prolonging the integration time is an effective way to improve the radar detection ability.

However, the range cell migration (RCM) and Doppler frequency migration (DFM) induced by the target motion during the long integration time cause integration gain loss and degrade the detection ability. A long-time hybrid coherent and noncoherent integration method is proposed to overcome such issues. This method uses the keystone transform and the matched filtering function H_1 to remove the linear RCM and quadratic RCM, respectively. Then, the long-time integration time is segmented into multiple frames with the same duration. Another matched filtering function H_2 is designed to eliminate the DFM. Finally, coherent integration and noncoherent integration operations are implemented inside and among the frames to improve the signal-to-noise ratio of the target-reflected GNSS signal available for detection. A maritime measurement campaign is conducted and confirms the effectiveness of the proposed method for sea target detection. Monte-Carlos trials and computational cost analysis show that the detection capability of the proposed method outperforms that of the existing methods but the computational cost is in the same order as $\mathcal{O}(N^3 \log N)$.

Keywords GNSS · Passive radar · Sea target detection · RCM and DFM correction · Hybrid coherent and noncoherent integration

Introduction

Global navigation satellite system reflectometry (GNSS-R) relies on using the GNSS reflection signals to remotely sense the geophysical and geometrical parameters of the earth's surface. Currently, the main applications of GNSS-R concentrate on ocean altimetry (Fagundes et al. 2021), wind speed retrieval (Guo et al. 2022), snow depth inversion (Hu et al. 2022), soil moisture retrieval (Al-Khaldi and Johnson. 2022), etc. Due to the global signal coverage and high space-time sampling of GNSS constellations, the reflected GNSS signals can also be used to continuously monitor the moving targets on the sea surface with a silent mode, which has a potential military application value.

Therefore, applying sea target detection using the GNSS reflection signals has attracted substantial attention from both remote sensing and radar research communities. Some investigations (Lu et al. 2013; Simone et al. 2017; Southwell et al. 2020) adopted the delay-Doppler maps (DDMs) with a conventional forward-scattering configuration for sea target detection. However, some problems arise from the DDMs with the forward-scattering configuration, such as weak secondary peak, strong sea clutter, ambiguous target geolocation, and rough spatial resolution. In this application, a back-scattering configuration is preferable to the forward-scattering one (Clarizia et al. 2015). In recent years, based on the back-scattering configuration, exploiting the radar signal processing technique to cope with sea target detection has become a research hotspot, i.e., a GNSS-based passive radar. However, the main shortcoming of GNSS-based passive radar is the restricted signal power density on the earth's surface. As a result, the target returns are extremely weak and submerged by the background noise, limiting the operational range of the radar. Therefore, improving the signal-to-noise ratio (SNR) of the target signal is the key point for sea target detection.

Long integration time is an effective way to enhance the SNR of the target signal. However, for the moving target on the sea surface, such as a ship, the target's motion cannot be neglected over the long integration time, which causes the target contributions to disperse on several resolution cells, involving the range cell migration (RCM) and Doppler frequency migration (DFM). The occurring migrations must be compensated to align the target contributions to achieve a proper integration gain available for reliable detection.

Some fully coherent integration methods have been proposed for GNSS-based passive radar to correct the occurring migrations. Wang et al. (2021) reported a long-time integration Fourier transform that can remove the DFM but ignore the RCM correction. Zhou et al. (2022) presented a modified radon Fourier transform that can handle both the RCM and DFM problems by jointly searching the range, Doppler frequency, and Doppler rate of the target. However, the typical coherent integration time is in the range of a few seconds because the ship decorrelation will occur for a

longer integration time (Pastina et al. 2021). Therefore, the detection capabilities of these fully coherent integration methods are restricted, suitable for short-range case. To improve the detection capability of GNSS-based passive radar, some long-time hybrid coherent and noncoherent integration methods have been suggested, whose integration time can be up to several tens of seconds. Their basic strategy is to divide the long integration time into consecutive frames with short durations. During each frame, the ship scattering mechanism can be regarded as coherent. Then, coherent and noncoherent integration operations are implemented inside and among the frames, respectively, to enhance the SNR of the target signal. Meanwhile, the RCM and DFM compensation operations are performed. Li et al. (2017) combined the keystone transform (KT) and the fractional Fourier transform (FrFT) for long-time hybrid integration. In this approach, the KT is used to correct the linear RCM, while the FrFT removes the DFM inside the frames and provides the coherent integration gain. Then, a Doppler frequency alignment operation is conducted to correct the DFM among the frames, followed by the noncoherent integration. Because the LV's distribution (LVD) can provide a higher signal concentration ratio and lower sidelobes than the FrFT, He et al. (2021) combine the KT and LVD to eliminate the RCM and DFM and offer hybrid integration gain. The above two approaches ignore the quadratic RCM compensation problem due to the rough range resolution of GPS L1 signal (The optimal range resolution is about 150 m). However, if a moving target is illuminated by the GNSS signal with a wider bandwidth (such as GPS L5 signal whose optimal range resolution is about 15 m) or a moving target has a higher speed, the integration loss induced by the quadratic RCM cannot be neglected and reduces the detection capability. Santi et al. (2017) proposed a local plane based technique that can remove the RCM and DFM without any approximation, allowing the highest integration gain. But this technique suffers from position and velocity ambiguity problems. Ma et al. (2018) adopted azimuth fast Fourier transform (FFT) to accomplish coherent integration inside the frames and proposed a target motion compensation (TMC) procedure that performs the RCM and DFM compensation among the frames by the tested Doppler rate values. However, the RCM and DFM problems inside the frames are ignored.

Inspired by the previous studies in GNSS-based passive radar, we propose a new long-time hybrid integration to improve the SNR for sea target detection. In the proposed method, the KT is employed to remove the linear RCM. Then, two matched filtering functions are designed to eliminate the quadratic RCM and the DFM inside and among the frames. Finally, coherent integration based on azimuth FFT and noncoherent integration operations are conducted. Both the field trial and simulation results confirm the effectiveness of the proposed method and show that the proposed method is superior to the existing hybrid integration methods (Li et al. 2017; Ma et al. 2018) for detection ability.

Characteristics of GNSS-based passive radar are introduced in the second section. The proposed method is described in the third section. The experimental and simulated results are provided next, followed by the conclusion and future work.

Characteristics of GNSS-based passive radar

This section first introduces the bistatic acquisition geometry of GNSS-based passive radar. Then, the signal models of both the direct and target signals are given. Finally, the theoretical target detection capability is discussed.

Bistatic acquisition geometry

The receiver system of GNSS-based passive radar shown in the top panel of Fig. 1 is a software-defined receiver, comprising two different types of antennas, a receiver front-end with two parallel channels, and the host computer. One channel of the receiver front-end is regarded as the reference channel (RC), connecting a right-hand circular polarization (RHCP) antenna to acquire the direct signal from the GNSS satellite as the reference signal. Another channel is the surveillance channel (SC), which adopts a high-gain left-hand circular polarization (LHCP) antenna to record the target signal from the moving ship because the reflection of a right-hand circularly polarized signal is a

predominantly left-hand circularly polarized signal in the back-scattering configuration (Zuo 2011). Both radio signals are transformed into digital intermediate frequency (IF) signals via the receiver front-end, convenient for the host computer processing.

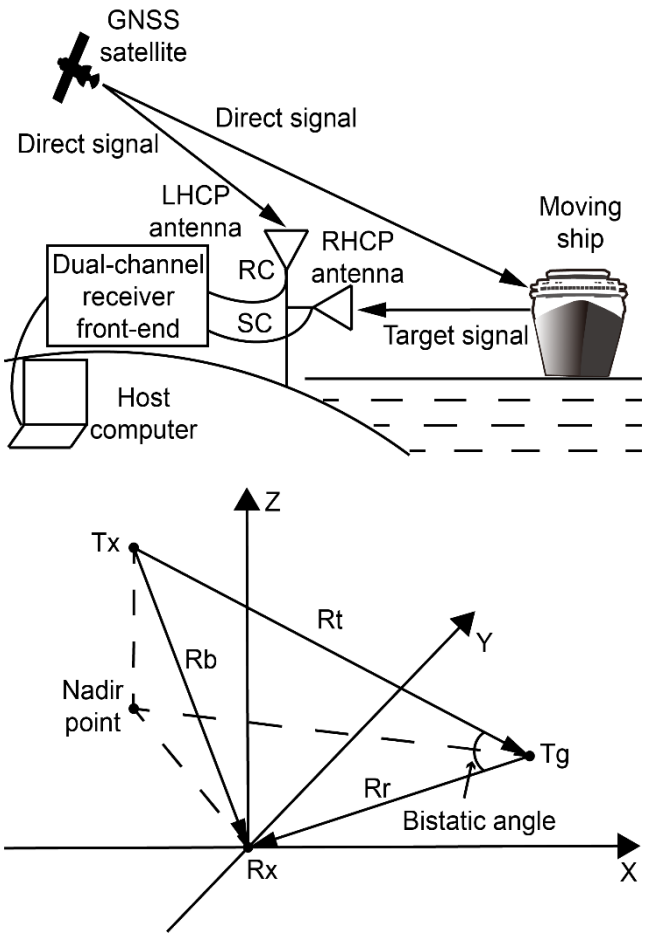

Fig. 1 GNSS-based passive radar receiver system fixed on the shore (top), and the corresponding bistatic acquisition geometry (bottom)

Based on the receiver system, the bottom panel of Fig. 1 gives the bistatic acquisition geometry of GNSS-based passive radar for sea target detection. We define the instantaneous ranges between satellite (Tx), receiver (Rx), and moving target (Tg) as follows: R_t is the Tx-Tg range, R_r is the Tg-Rx range, and R_b is the baseline range between Tx and Rx. Because the passive radar system obtains the range-compressed signal by matched filtering with the direct signal compensating the

instantaneous delay between the Tx and Rx, the bistatic range history of the Tg is defined as:

$$R_{bi}(t) = R_t(t) + R_r(t) - R_b(t) \quad (1)$$

where t is the observation time.

Signal model

GNSS signal is a continuous wave, whose simplified expression can be written as:

$$S(t) = A \times C(t) \times D(t) \times \cos(2\pi f_c t + \varphi_{ini}) \quad (2)$$

where A is the signal amplitude, $C(\cdot)$ is the ranging code, $D(\cdot)$ is the navigation message, f_c is the central carrier frequency, and φ_{ini} is the initial carrier phase. Due to the low power density of the GNSS signal on the earth's surface, the direct signal collected by the RC is contaminated by the background noise, whose SNR can be as low as -30 dB (He et al. 2022). To overcome such a problem, signal synchronization (Antoniou and Cherniakov. 2013) is a crucial step, which can be achieved by the software receiver. The software receiver contains two main functions: signal acquisition and signal tracking. First, the signal acquisition function must determine whether the direct signals from all visible satellites are captured. Then, the signal tracking function is responsible for tracking the observation parameters of the direct signal, including code delay, carrier Doppler frequency, carrier phase, navigation data, etc. These observation parameters can generate a noise-free replica of the direct signal as the reference signal. For sea target detection, the 1-dimensional (1-D) reference signal has to be converted into the 2-D radar data format in terms of the equivalent pulse repetition interval (PRI) that can be matched to the ranging code length. After quadrature demodulation, ignoring constant phase and amplitude terms, the reference signal can be expressed as:

$$S_{di}(\tau, u) = C[\tau - \tau_{di}(u) - \tau_e(u)] \times D[\tau - \tau_{di}(u) - \tau_e(u)] \times exp\{j[2\pi f_{di}(u)\tau + \varphi_{di}(u) + \varphi_e(u)]\} \quad (3)$$

where $\tau \in [0, PRI]$ is the fast-time, $u \in \left[-\frac{T_{obv}}{2}, \frac{T_{obv}}{2}\right]$ is the slow-time, T_{obv} is the entire observation time. $\tau_{di}(u) = \frac{R_b(u)}{c}$, $\varphi_{di}(u) = -2\pi \frac{R_b(u)}{\lambda}$, and $f_{di}(u)$ are the instantaneous code delay, carrier phase, and Doppler frequency of the direct signal, respectively. c is the speed of light, and λ is the central carrier wavelength. $\tau_e(u)$ and $\varphi_e(u)$ are the total delay and phase errors, respectively, induced by the atmospheric factors and the receiver clock errors. Likewise, supposing one target, the reflected target signal can be written as:

$$S_{re}(\tau, u) = C[\tau - \tau_{re}(u) - \tau_e(u)] \times D[\tau - \tau_{re}(u) - \tau_e(u)] \times exp\{j[2\pi f_{re}(u)\tau + \varphi_{re}(u) + \varphi_e(u)]\} \quad (4)$$

where $\tau_{re}(u) = \frac{R_t(u)+R_r(u)}{c}$, $\varphi_{di}(u) = -2\pi \frac{R_t(u)+R_r(u)}{\lambda}$, and $f_{re}(u)$ are the instantaneous code delay, carrier phase, and Doppler frequency of the target signal, respectively. However, the values of the navigation message give rise to a phase change of +180 or -180 degrees, limiting the coherent integration time within 20ms. To extend the coherent integration time, the navigation message in (4) should be removed. Moreover, the delay and phase errors in (4) should also be eliminated. Fortunately, the navigation message in both (3) and (4) are the same within the range of 6000 km (Zeng. 2013). The delay and phase errors in both (3) and (4) are very close to each other due to the similar atmospheric factors and the shared oscillator between the RC and SC. We can remove the above interference factors by the following range compression.

Range compression is conducted in the fast-time domain by the cross-correlation between the reference signal in (3) and the target signal in (4). After range compression, the range-compressed signal can be expressed as:

$$rc(\tau, u) = cf\left[\tau - \frac{R_{bi}(u)}{c}\right] \times exp\left[-j2\pi \frac{R_{bi}(u)}{\lambda}\right] \quad (5)$$

where $cf(\cdot)$ denotes the envelope of the cross-correlation function. In this study, a moving target with almost constant velocity is assumed. This assumption is reasonable for sea ships sailing at cruising speeds (Li et al. 2017; Ma et al. 2018). Due to the fact

that R_t and R_b (more than 20,000 km) are much greater than R_r, the bistatic range in (1) can be expanded into the second-order Taylor series as follows:

$$R_{bi}(u) = \lambda \times \frac{\gamma}{2} \times u^2 + \lambda f_{cen} \times u + R_{ini} \tag{6}$$

where γ is the Doppler rate, f_{cen} is the Doppler centroid, R_{ini} is the initial bistatic range. Substituting (6) into (5), the range-compressed signal can be rewritten as:

$$rc(\tau, u) = cf\left[\tau - \frac{\lambda \times \frac{\gamma}{2} \times u^2 + \lambda f_{cen} \times u + R_{ini}}{c}\right]$$

$$\times exp\left[-j2\pi\left(\frac{\gamma}{2} \times u^2 + f_{cen} \times u + \frac{R_{ini}}{\lambda}\right)\right] \tag{7}$$

As shown in (7), the envelope of the cross-correlation function is coupled with the slow-time, leading to the RCM, and the exponential phase term is a quadratic phase function with respect to the slow-time, resulting in the DFM. Both the RCM and DFM make the target energy defocusing over the long integration time. Therefore, they must be compensated before coherent and noncoherent integration.

Target detection capability analysis

According to the bistatic radar equation (Cherniakov. 2008), the SNR of the range-compressed signal can be derived as:

$$SNR_{rc} = \rho_{pfd} \times \frac{\sigma\lambda^2 G_s}{(4\pi R_r)^2 L_s} \times \frac{PRI \times B_\omega}{KT_0 B_n F_0} \tag{8}$$

where ρ_{pfd} is the power flux density on the earth's surface produced by the GNSS satellite, σ is the bistatic radar cross section (RCS) of the moving target, G_s is the LHCP antenna gain, L_s is the system loss, B_ω is the ranging code bandwidth, K is the Boltzmann constant, T_0 is the receiver noise temperature, B_n is the receiver noise bandwidth, F_0 is the noise factor. Table 1 lists the values of the parameters in (8). It should be noted that the value of ρ_{pfd} originates from Shi et al. (2017), while the receiver parameters are from the receiving hardware used in the following field trials. In terms of (8), the top panel of Fig. 2 plots the variation in the SNR of range-

compressed signal with R_r for different values of RCS. Although the GNSS signal's ranging code can offer cross-correlation gain via range compression, the SNR values of the range-compressed signal are still very low. For a target with 5 km R_r and 1000 m^2 RCS, its SNR is only about -33 dB, much lower than the detection threshold of 10.7dB that is used for reliable detection with a detection probability of 0.9 (Richards. 2014).

Table 1 GNSS and receiver parameters used for the SNR calculation

Parameters	Values	Parameters	Values
P_{pfd}(dBW/m^2)	-135	K(J/K)	1.38×10^{-23}
λ(m)	0.19	T_0(K)	290
B_ω(MHz)	1.023	B_n(MHz)	1.023
PRI(ms)	1	F_0(dB)	1.49
σ(m^2)	500,1000,1500	G_s(dB)	12
R_r(km)	0.5-10	L_s(dB)	2

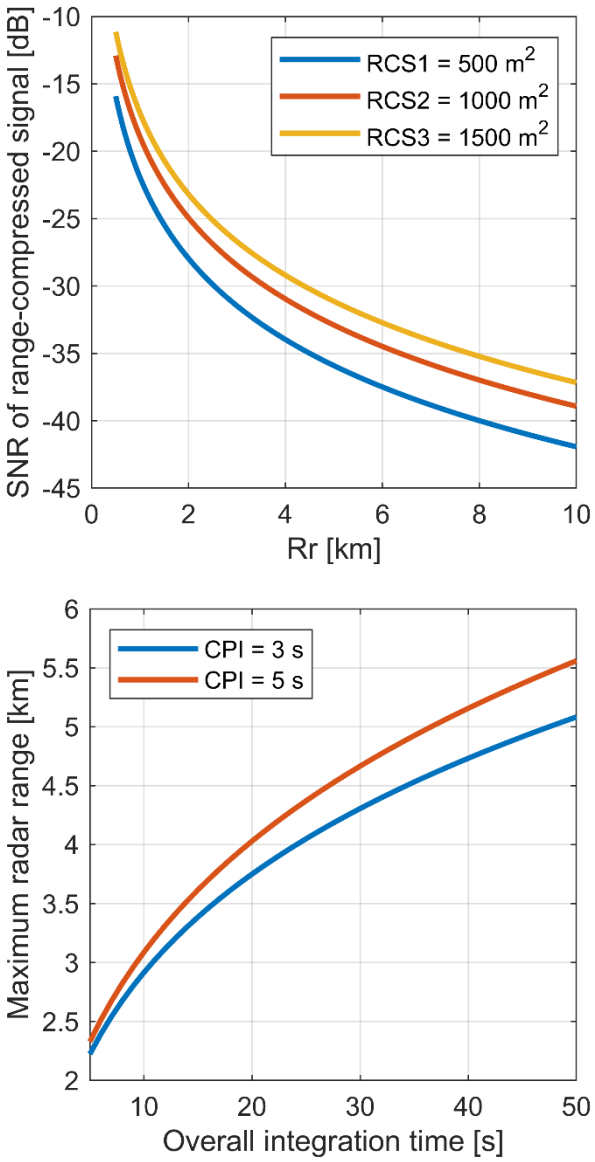

239

240 **Fig. 2** Variation in the SNR of range-compressed signal with R_r for different values
241 of RCS in the case of GPS L1 signal (top) and the variation in the maximum radar range
242 with the overall integration time for different values of CPI in the case of 1000m^2 RCS
243 (bottom)

244

245 Prolonging the integration time is an effective way to enhance the SNR for reliable
246 detection. Due to the target RCS decorrelation over the long integration time (Pastina
247 et al. 2021), the strategy of hybrid coherent and noncoherent integration is adopted here.
248 First, the long integration time is segmented into M frames. Each frame has an

identical and short coherent processing interval (CPI). Then, coherent integration and noncoherent integration operations are implemented inside and among the frames, respectively. After hybrid integration, the improved SNR of the range-compressed signal can be obtained as:

$$SNR_{im} = SNR_{rc} \times G_{CI} \times G_{NCI} \tag{9}$$

$$G_{CI} = CPI, G_{NCI} \approx \sqrt{M}$$

where G_{CI} is the coherent integration gain, G_{NCI} is the noncoherent integration gain. Substituting (8) into (9), the maximum radar range can be derived as:

$$(R_r)_{max} = \sqrt{\rho_{pfd} \times \frac{\sigma\lambda^2 G_s B_\omega PRI}{(4\pi)^2 K T_0 B_n F_0 L_s SNR_{im}} \times G_{CI} \times G_{NCI}} \tag{10}$$

In terms of (10), the variation in the maximum radar range with the overall integration time for different values of CPI is presented in the bottom panel of Fig. 2. It can be found that with the integration time increasing, the maximum radar range is extended. Furthermore, the larger value of CPI can yield a longer maximum radar range. However, the RCM and DFM caused by the target motion give rise to the hybrid integration gain loss, reducing the target detection range. In the following section, the RCM and DFM issues will be addressed.

Long-time hybrid integration method

A new hybrid integration method is proposed here, including the RCM and DFM corrections and hybrid integration. In addition, the computational cost of the proposed method is analyzed and compared with the existing methods (Li et al. 2017; Ma et al. 2018).

RCM correction

In order to cope with the RCM, the range-compressed signal in (7) is transformed into

the range-frequency and slow-time domain by the range FFT, which is obtained as:

$$rc(f_\tau, u) = CF(f_\tau) \times exp\left[-j2\pi\left(\frac{\gamma}{2} \times \frac{f_\tau + f_c}{f_c} \times u^2 + f_{cen} \times \frac{f_\tau + f_c}{f_c} \times u + \frac{f_\tau + f_c}{c} \times R_{ini}\right)\right] \tag{11}$$

where f_τ is the range-frequency, $CF(\cdot)$ is the Fourier transform of $cf(\cdot)$. Equation (11) indicates that the range frequency is coupled with u-term and u^2-term, resulting in the linear RCM and quadratic RCM.

We can use the KT to remove the linear RCM by a scaling operation:

$$(f_\tau + f_c) \times u = f_c \times u' \tag{12}$$

where u' is the rescaled slow-time. Substituting (12) into (11), we have:

$$rc(f_\tau, u') = CF(f_\tau) \times exp\left[-j2\pi\left(\frac{\gamma}{2} \times \frac{f_c}{f_\tau + f_c} \times u'^2 + f_{cen} \times u' + \frac{f_\tau + f_c}{c} \times R_{ini}\right)\right] \tag{13}$$

It can be found from (13) that the range frequency is still coupled with the u'^2-term after the KT implementation due to the quadratic RCM.

Because the narrow band of GNSS ranging code makes $f_\tau \ll f_c$, according to the Taylor series expansion around the range frequency, we get

$$\frac{f_c}{f_\tau + f_c} \approx 1 - \frac{f_\tau}{f_c} \tag{14}$$

Substituted (14) into (13), equations (13) can be rewritten as:

$$rc(f_\tau, u') = CF(f_\tau) \times exp\left[-j2\pi\left(\frac{\gamma}{2} \times u'^2 + f_{cen} \times u' + \frac{f_\tau + f_c}{c} \times R_{ini}\right)\right] \times exp\left(j\pi \times \gamma \times \frac{f_\tau}{f_c} \times u'^2\right) \tag{15}$$

To eliminate the residual quadratic RCM in (15), the matched filtering function H_1 is constructed in the range-frequency and slow-time domain, which is expressed as:

$$H_1(f_\tau, u'; \gamma^*) = exp\left(-j\pi \times \gamma^* \times \frac{f_\tau}{f_c} \times u'^2\right) \tag{16}$$

where γ^* is the tested Doppler rate. When the tested parameter matches the true Doppler rate, the coupling effects between the range frequency and slow-time can be removed by multiplying (15) by (16).

After the range inverse FFT (IFFT) implementation, the range-compressed signal is segmented into successive M frames with respect to the slow-time, which can be expressed as:

$$rc^m(r,u';\gamma^*) = CF(r - R_{ini};\gamma^*) \times rect\left(\frac{u' - m \cdot T_f}{T_f}\right)$$

$$\times exp\left[-j2\pi\left(\frac{\gamma}{2} \times u'^2 + f_{cen} \times u' + \frac{R_{ini}}{\lambda}\right)\right] \quad (17)$$

where $r = \tau \times c$ is the bistatic range cell, $rect(\cdot)$ is the time window, $m \in \left[-\frac{M}{2}, \frac{M}{2} - 1\right]$, $T_f = \frac{T_{obv}}{M}$ is the length of CPI. It can be seen from (17) that the target's envelope is now aligned within one bistatic range cell because both the linear RCM and quadratic RCM have been corrected. Therefore, the following processing with respect to the slow-time can be conveniently performed for each bistatic range cell.

DFM Correction and Hybrid Integration

Before the hybrid integration, the DFM inside each frame and among multiple frames must be compensated. Since the tested Doppler rate γ^* has been exactly matched in the previous subsection, the DFM inside the m-th frame can be corrected by:

$$\delta f_d^m(u';\gamma^*) = \gamma^* \times (u' - u'_m) \times rect\left(\frac{u' - m \cdot T_f}{T_f}\right) \quad (18)$$

where u'_m represents the reference slow-time in the m-th frame.

Likewise, the DFM from the m-th frame to the reference frame ($m = 0$) can be corrected by:

$$\Delta f_d^m(\gamma^*) = f_d^m - f_d^0 = \gamma^* \times m \times T_f \quad (19)$$

In terms of (18) and (19), the matched filtering function H_2^m is constructed in the range and slow-time domain to remove the DFM inside and among the frames, which is obtained as:

$$H_2^m(r,u';\gamma^*) = rect\left(\frac{u'-m\cdot T_f}{T_f}\right)\times$$

$$exp\left\{-j2\pi\left[\frac{1}{2}\times\delta f_d^m(u';\gamma^*)+\Delta f_d^m(\gamma^*)\right]\times(u'-u'_m)\right\} \quad (20)$$

After multiplying (17) by (20), coherent integration inside each frame can be conducted by the azimuth FFT along the slow-time.

Finally, all frames can be noncoherently integrated. We obtain the integrated range-Doppler map (RD map) as:

$$RD_{INT}(r,f_d;\gamma^*) = \frac{1}{M}\sum_{-\frac{M}{2}}^{\frac{M}{2}-1}\|RD_m(r,f_d;\gamma^*)\| \quad (21)$$

where f_d is the Doppler frequency. The presence of the moving target in the integrated RD map can be determined by the detector of the 2-D cell averaging constant false alarm rate (CA-CFAR) (Richards. 2014). The whole processing procedure of the proposed method is summarized in Fig. 3.

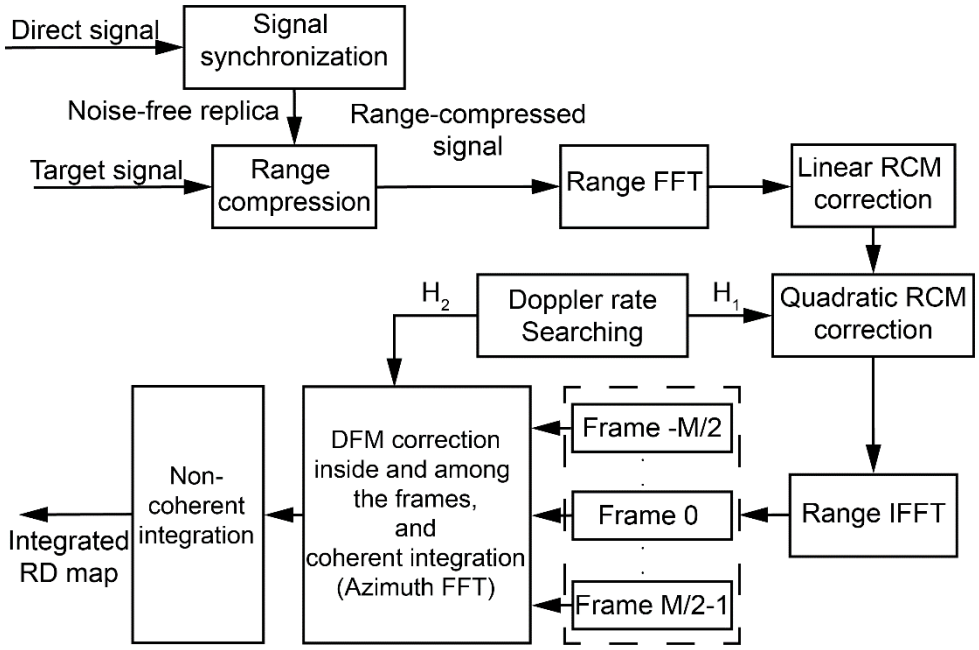

Fig. 3 Flowchart of the proposed long-time hybrid integration method, including five main steps of signal synchronization, range compression, RCM correction, DFM correction, and hybrid integration

Computational cost analysis

In this subsection, the computational cost of the proposed method is analyzed. It should be noted that since signal synchronization, range compression, and noncoherent integration are the common steps in the existing methods (Li et al. 2017; Ma et al. 2018), the computational costs of these steps are not taken into account here.

Assume that N_r, N_t, $N_t' = \frac{N_t}{M}$, N_c, and N_a denote the number of range cells, the number of slow-time samples, the number of CPI samples, the number of tested Doppler rates, and the number of rotation angles (Li et al. 2017). As shown in the previous subsections, the RCM correction, DFM correction, and coherent integration account for the main computational cost of the proposed method, requiring multiple FFT or IFFT operations. Suppose that the calculation of FFT or IFFT over n needs the computational cost in the order of $\mathcal{O}(N \log N)$. Because the KT can be implemented by a fast algorithm, i.e., chirp-Z-transform and IFFT (CZT-IFFT) (Wang et al. 2013),

the total computational cost of the KT and the matched filtering function H_1 used for the RCM correction is $\mathcal{O}(4N_rN_t\log N_t + N_rN_t\log N_r + N_cN_rN_t\log N_r)$. Because the matched filtering function H_2 eliminates the DFM followed by the azimuth FFT, the total computational cost of the DFM correction and coherent integration is $\mathcal{O}(N_cN_rN_t\log N_t')$. Table 2 summarizes the overall computational cost of the proposed method, also including two existing methods. It can be seen that the computational costs of the three methods are in the same order of $\mathcal{O}(N^3\log N)$ under the assumption of $N_r = N_t = N_t' = N_c = N_a = N$.

Table 2 Computational cost of the three methods

Methods	Computational cost
TMC+FFT (Ma et al. 2018)	$\mathcal{O}(N_cN_rN_t\log N_t' + 2N_cN_rN_t\log N_r)$
KT+FrFT (Li et al. 2017)	$\mathcal{O}(4N_aN_rN_t\log N_t' + 4N_rN_t\log N_t + 2N_rN_t\log N_r)$
The proposed method	$\mathcal{O}(N_cN_rN_t\log N_t' + N_cN_rN_t\log N_r + 4N_rN_t\log N_t + N_rN_t\log N_r)$

Experiments

In this section, field trials and simulation experiments are carried out to validate the effectiveness of the proposed method and to compare the detection capability of the proposed method with the existing methods.

Field trial results

A maritime experiment was carried out at Cyberport Waterfront Park in Hong Kong on May 16, 2019. The data acquisition geometry of the field trial is presented in the top panel of Fig. 4, where the Rx was deployed on the shore, recording the direct and reflected signals simultaneously. The middle panel shows the receiving hardware, comprising the dual-channel receiver front-end, circular and square antennas, and the host computer. The circular antenna is a commercial off-the-shelf RHCP antenna pointing towards the sky for direct signal collection. While the square antenna is a custom LHCP antenna with a 12dB gain steering towards the sea surface for target signal collection. The receiver front-end converts both radio signals into digital IF signals for the host computer processing. A moving cargo ship was selected as the target of interest, whose trajectory crossed the line of sight of the LHCP antenna as shown in the top panel of Fig. 4. The bottom panel gives the photograph of the cargo ship, including the ship name and time when the ship passed through the field of view of the receiving hardware. The automatic identification system (AIS) provided the voyage-related information of the cargo ship. Two GPS satellites were employed as illuminators of opportunity. Table 3 gives the relevant experimental parameters and Table 4 includes the AIS parameters of the cargo ship and satellite information.

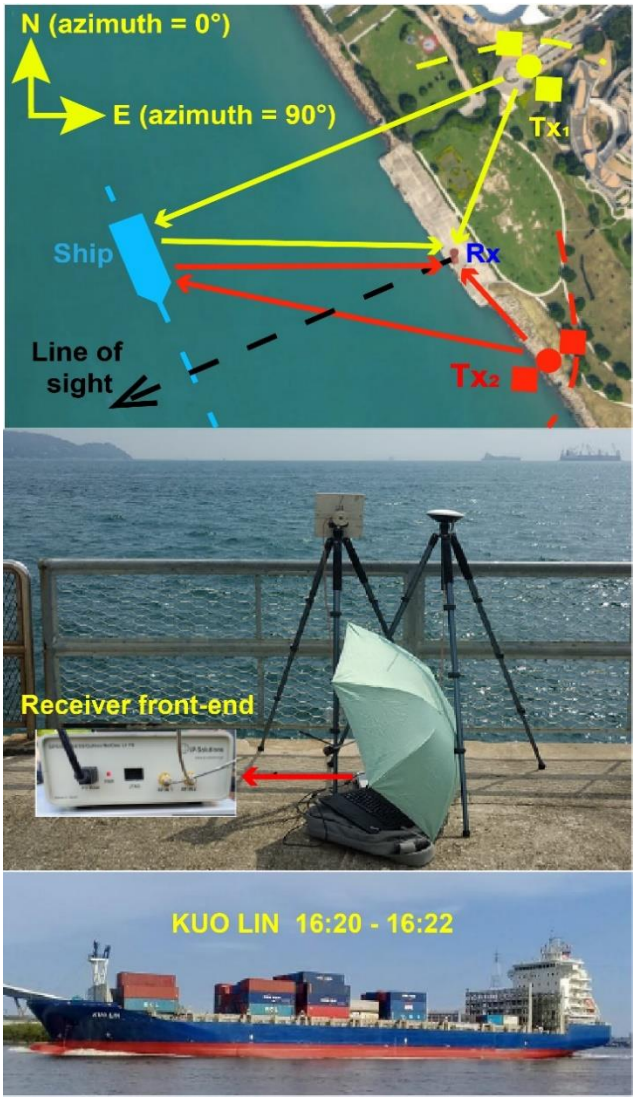

Fig. 4 Data acquisition geometry of the field trial (top), the receiving hardware (middle), and photography of the moving cargo ship (bottom)

Table 3 Experimental parameters

Parameters	Values
Carrier frequency (MHz)	1575.42
Ranging code bandwidth (MHz)	1.023
PRI (ms)	1

Sampling rate (MHz)	16.368
Observation time (ms)	114,688
CPI (ms)	2048
Noncoherent integration times	56

Table 4 AIS information and satellite information

Ship name	Ship length (m)	Speed (m/s)	Shortest range to Rx (m)
KUO LIN	170	7.52	783.6
Satellite	Ranging code	Elevation angle (°)	Azimuth angle (°)
GPS BIIF-8	PRN 03	41	71
GPS BIIR-10	PRN 22	25	53

In order to detect the moving cargo ship in the RD map, the conventional moving target detection (cMTD) technique (Richards 2014) is first adopted. This technique is implemented by azimuth FFT inside each frame to provide coherent integration gain. Then, all frames are noncoherently integrated without any motion compensation. The top and bottom panels of Fig. 5 show the resulting RD maps with respect to two GPS satellites. The color scales are in dB, where 0 dB is the mean power of the background noise. As can be seen, the sidelobes of the compressed direct signal (recorded by the sidelobes of LHCP antenna) well-focused along the zero-Doppler frequency line have the strongest intensity in both RD maps. They are regarded as static strong returns and can be directly filtered out. But we retain them to compare with the target contributions.

Due to the long integration time, the motion of the cargo ship cannot be ignored, which changes the positions of the target contributions in the RD maps, leading to the RCM and DFM. As a result, it is apparent that the target contributions are spread over several RD cells and submerged by the static strong returns in the top and bottom panels of Fig. 5.

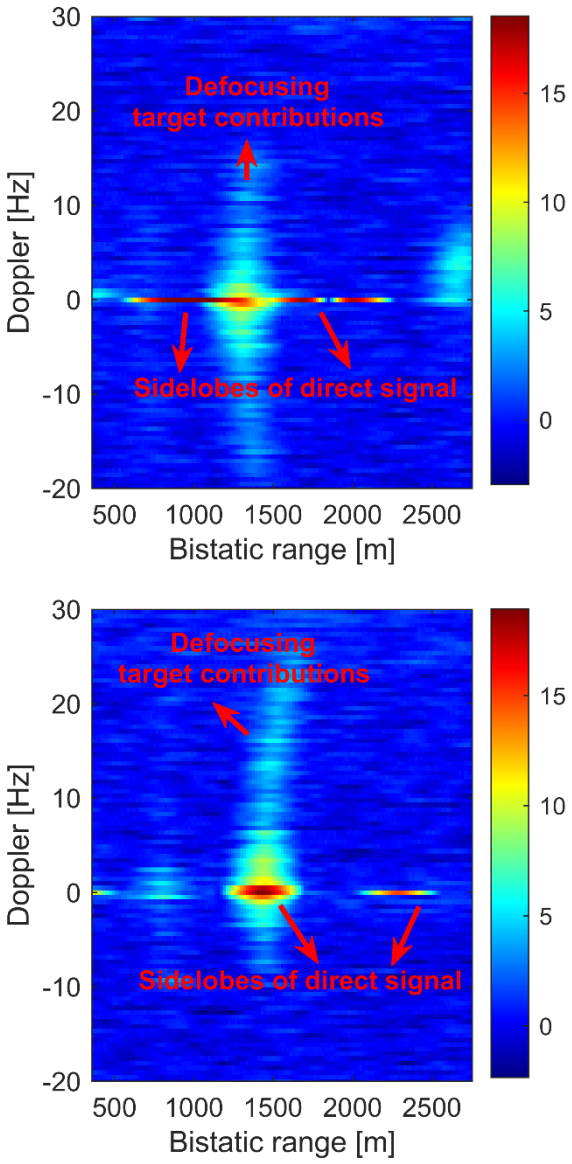

Fig. 5 Resulting RD maps of the moving cargo ship available from the cMTD technique by using GPS PRN03 (top) and GPS PRN22 (bottom) as the illuminators of opportunity.

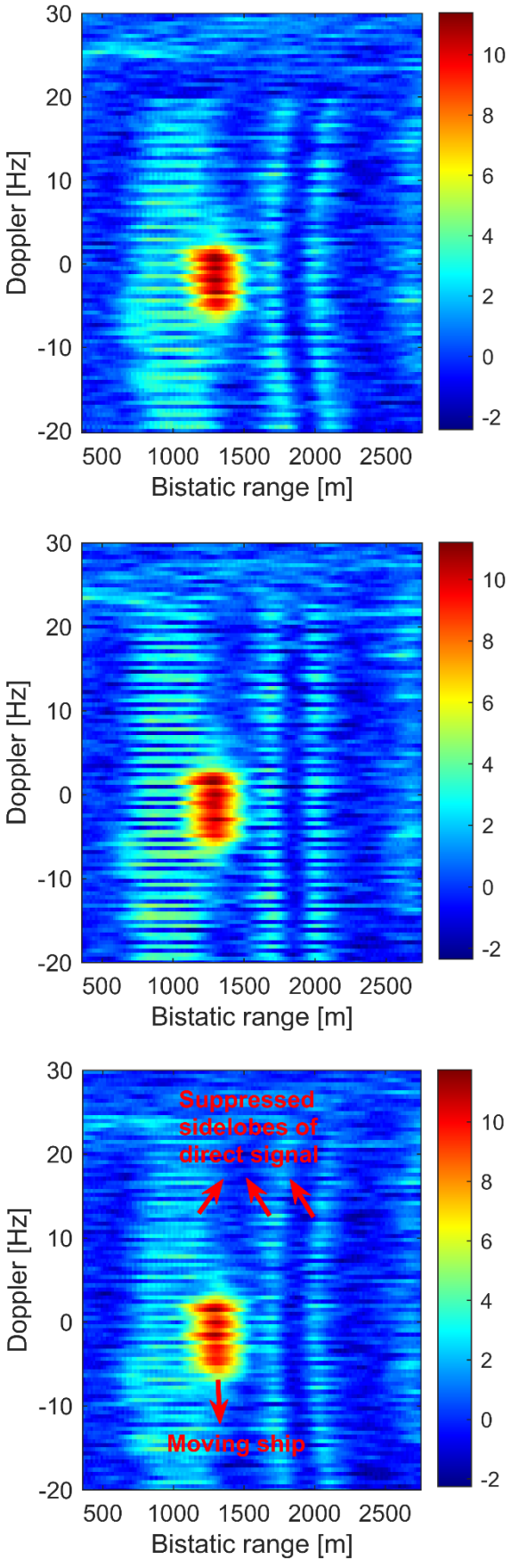

415

416 **Fig. 6** Resulting RD maps of the moving cargo ship available from the TMC+FFT (top),

417 the KT+FrFT (middle), and the proposed method (bottom) by using GPS PRN03 as the
418 illuminator of opportunity.
419

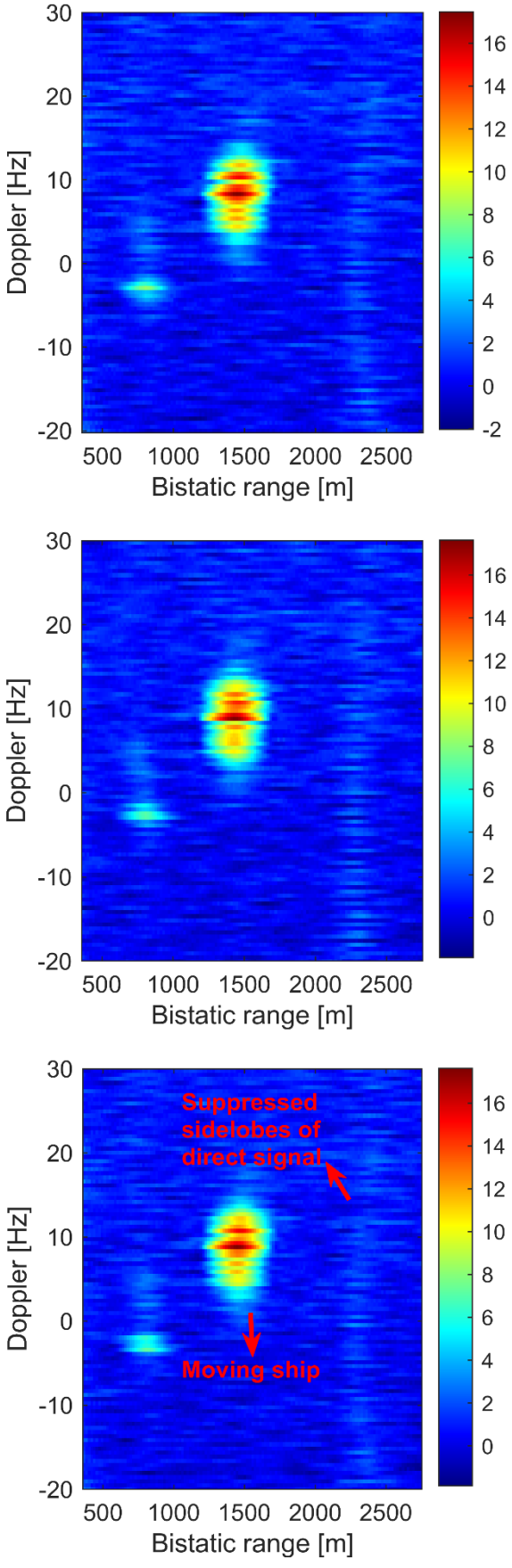

Fig. 7 Resulting RD maps of the moving cargo ship available from the TMC+FFT (top),

the KT+FrFT (middle), and the proposed method (bottom) by using GPS PRN22 as the illuminator of opportunity.

As shown in the top and bottom panels of both Figs. 6 and 7, the target contributions corresponding to the three methods are easily distinguished from the background noise. The highest intensity values of the target contributions are more than 10 dB, sufficient for reliable detection. The main reasons are as follows. On the one hand, the target energy has been focused since the three methods perform the RCM and DFM compensations and provide adequate hybrid integration gain. On the other hand, the three methods can defocus the energy of the static strong returns into several RD cells. Hence, compared with the top and bottom panels of Fig. 5, the sidelobes of the compressed direct signal in the top and bottom panels of Figs. 6 and 7 have been dramatically suppressed. The effectiveness of the three methods for sea target detection can be confirmed by two experimental data sets. However, because the trajectory of the cargo ship is nearly orthogonal to the line of sight of the LHCP antenna in the real experiment, leading to a low radial velocity of the target relative to the Rx, the RCM and DFM are not severe inside each frame. Therefore, the highest intensity values of the target contributions are close to each other in the top and bottom panels of Figs. 6 and 7. It is difficult to visibly compare the detection capabilities of the three methods. Simulation experiments are implemented in the following to address this issue. Furthermore, due to the short-range experimental validation case, the cargo ship cannot be regarded as a point-like target. Therefore, the focused target contributions occupy the ranges of Doppler frequencies in the top and bottom panels of Figs. 6 and 7, which implies that it is possible to estimate the ship length. However, this is beyond the scope of this study.

Simulation results

In the simulation experiments, a point-like moving target is considered, and additive

white Gaussian noise is used as the background disturbance. GNSS and receiver parameters are identical to Table 1, while the simulation parameters of both the moving target and signal processing are given in Table 5. According to the block diagram of Fig. 8, the simulation experiments are implemented to evaluate the detection capabilities of the four approaches as mentioned above.

Table 5 Simulation parameters

	Parameters	Values
Target	Speed (m/s)	10
	Doppler rate (Hz/s)	-0.9806
	Initial range (m)	4250
	Range-compressed SNR (dB)	-19.47
Signal Processing	Integration time (ms)	40,960
	CPI (ms)	4096
	Noncoherent integration times	10

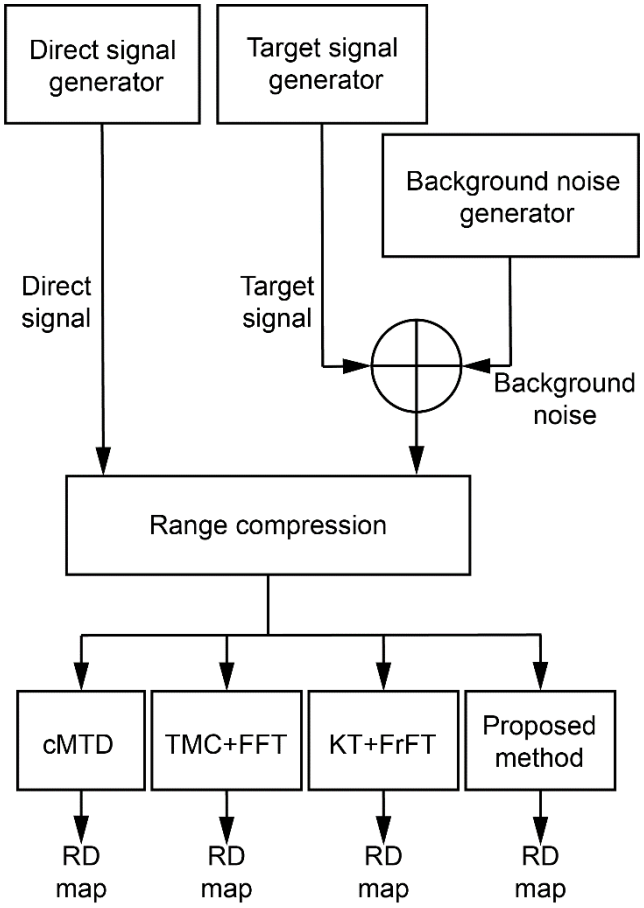

458

459 **Fig. 8** Processing chain of the simulation experiments, including the simulated data
460 generation and the implementation of the cMTD, the TMC+FFT, the KT+FrFT, and
461 the proposed method.

462

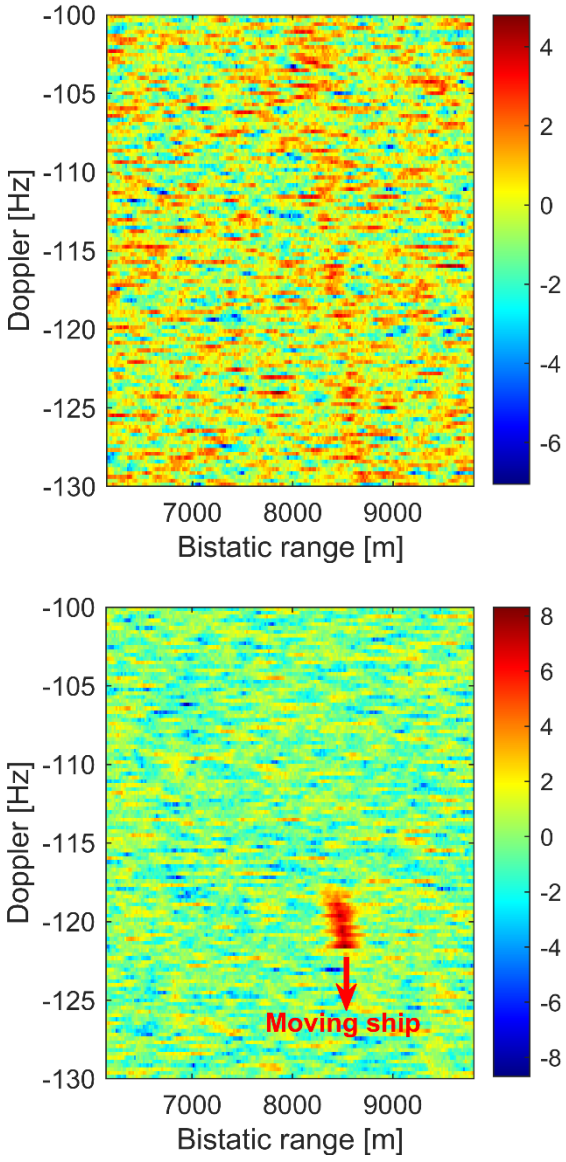

463

464 **Fig. 9** Simulated RD maps available from the cMTD technique (top) and the TMC+FFT
465 (bottom)

466

467 From the top panel of Fig. 9, it can be seen that the background noise buries the
468 moving target because the cMTD technique cannot handle the RCM and DFM issues,
469 resulting in the integration gain loss. In the bottom panel, although we can visually
470 separate the target contributions from the background noise, the target contributions are
471 defocused along the Doppler frequency dimension because the high Doppler frequency
472 resolution (1/CPI) does not allow the DFM inside the frame to be neglected. On the

contrary, the top and bottom panels of Fig. 10 demonstrate the well-focused target contributions in the RD maps due to the RCM and DFM correction provided by the KT+FrFT and the proposed method. The top panel of Fig. 11 plots the range profiles of the RD maps in the top and bottom panels of both Fig. 9 and Fig. 10 around their peaks with the strongest intensities. Obviously, the intensity value of the peak pertaining to the proposed method exceeds 15dB, higher than that pertaining to the existing methods. The main reasons are as follows. Compared with the TMC+FFT, the proposed method corrects both the RCM and DFM inside each frame. While compared with the KT+FrFT, the quadratic RCM correction issue is solved by the proposed method. Therefore, the proposed method enables lower integration gain loss with the same length of CPI and overall integration time.

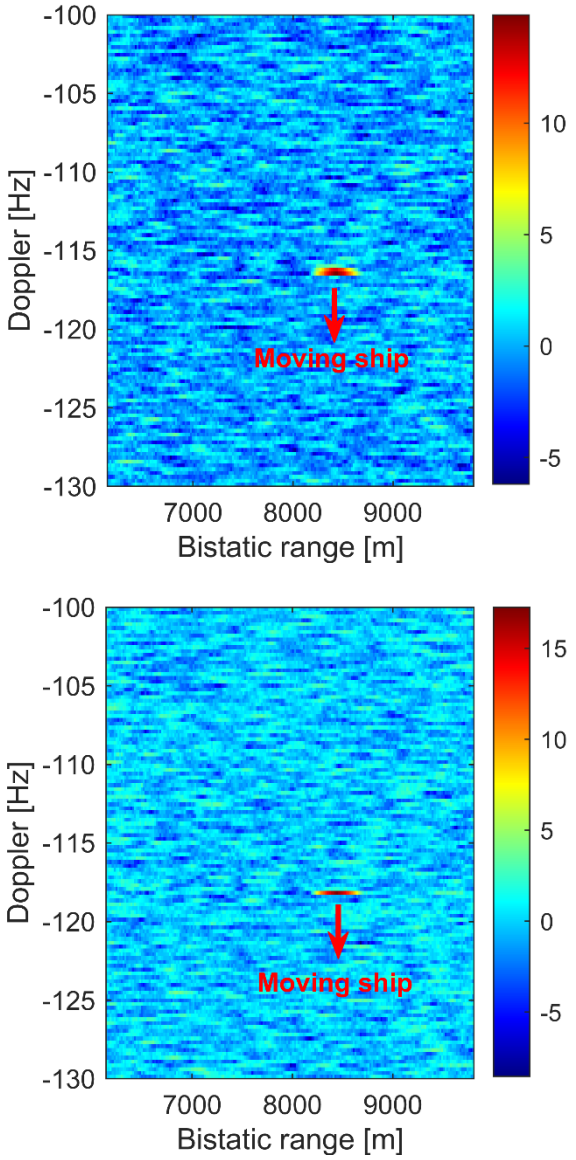

485

486 **Fig. 10** Simulated RD maps available from the KT+FrFT (top) and the proposed
487 method (bottom)

488

489 To quantitatively test the detection capabilities of the cMTD, the TMC+FFT, the
490 KT+FrFT, and the proposed method, Monte-Carlo trials are performed by adding the
491 randomly generated white Gaussian noise with different SNR levels into the target
492 signals, whose simulation parameters are the same as in Tables 1 and 5. The 2-D CA-
493 CFAR detector and the above four approaches are combined as the corresponding
494 detectors. The false alarm rate is set as $P_{fa} = 10^{-3}$, and 100 Monte-Carlo trials are done.

The bottom panel of Fig. 11 plots the curves of numerical detection results. As can be seen, for the same detection probability, the required SNR of the proposed method is lower than that of the existing methods. In other words, referring to the top panel, the detection range of the cMTD technique, the TMC+FFT, the KT+FrFT, and the proposed method are less than 500 m, about 1400 m, about 4200 m, and about 4600 m, respectively, for the 1000m^2 target RCS and the detection probability of 0.9. Therefore, the detection capability of the proposed method outperforms the existing methods in the case of exploiting the GNSS signal with the same bandwidth, thanks to its ability to correct the linear and quadratic RCM and the DFM inside and among the frames.

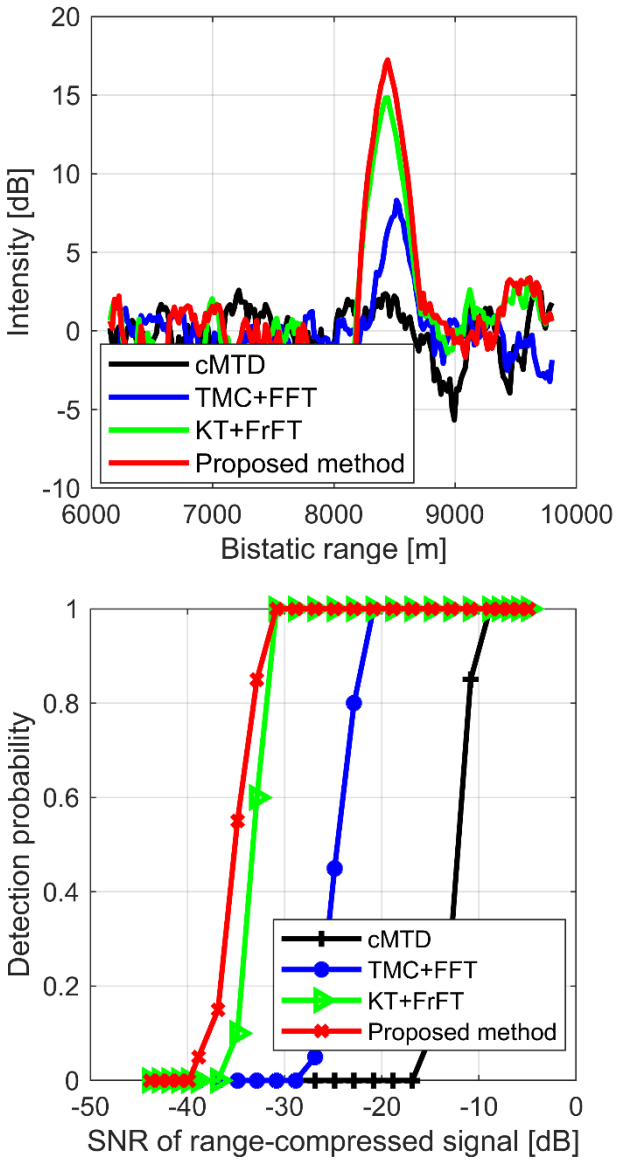

Fig. 11 Range profiles of the RD maps available from the four approaches (top), and the detection probabilities of four methods versus different SNR levels of the range-compressed signal (bottom)

Conclusion and future work

This study exploits the GNSS reflection signal to form a passive radar system for sea target detection. Due to the weak target echoes, a long-time hybrid integration method is proposed to improve the SNR of the moving target for reliable detection. In this method, the KT and two matched filtering functions are used to solve the RCM and DFM issues, which result in the hybrid integration gain loss and decrease the detection range. The computational cost analysis shows that the proposed and existing methods (Li et al. 2017; Ma et al. 2018) are in the same order. Field trials confirm the effectiveness of the proposed method and Monte-Carlo trials present that the detection capability of the proposed method is superior to the existing methods.

This study considers the sea-moving target with a constant velocity. However, for a maneuvering target, the detection performance of the proposed method will be affected. Therefore, our future work considers developing the proposed method for maneuvering target detection. More sophisticated processing will be needed.

Acknowledgments: The authors thank the anonymous reviewers for their helpful comments. This work was partly supported by the Natural Science Foundation of Jiangsu Province under Grant BK20221499 and partly by the University Grants Committee of Hong Kong under project R5009-21.

Data Availability The GNSS direct signal data and reflection signal data in the real experiments were collected by a GNSS SDR receiver "iP-Solutions" purchased at (http://www.ip-solutions.jp).

References

Al-Khaldi M, Johnson T (2022) Soil Moisture Retrievals Using CYGNSS Data in a Time-Series Ratio Method: Progress Update and Error Analysis. IEEE Geosci Remote Sens Lett, 19: 1-5. https://doi.org/10.1109/LGRS.2021.3086092

Antoniou M, Cherniakov M (2013) GNSS-Based Bistatic SAR: a Signal Processing View. EURASIP J Adv Signal Process, 2013(1): 1-16. https://doi.org/10.1186/1687-6180-2013-98

Cherniakov M (2008) Bistatic Radar: Emerging Technology. Hoboken, NJ, USA.

Clarizia M, Braca P, Ruf S, Willett P (2015) Target Detection Using GPS Signals of Opportunity. In: 18th International Conference on Information Fusion (Fusion), Washington, DC, 6-9 July, pp 1429-1436.

Fagundes R, Mendonça-Tinti I, Iescheck L, Akos M, Geremia-Nievinski F (2021) An open-source low-cost sensor for SNR-based GNSS reflectometry: design and long-term validation towards sea-level altimetry. GPS Solut, 25(2): 73-83. https://doi.org/10.1007/s10291-021-01087-1

Guo W, Du H, Cheong W, Southwell B, Dempster A (2022) GNSS-R Wind Speed Retrieval of Sea Surface Based on Particle Swarm Optimization Algorithm. IEEE Trans Geosci Remote, 60: 1-14. https://doi.org/10.1109/TGRS.2021.3082916

He Z, Yang Y, Chen W (2021) A hybrid integration method for moving target detection with GNSS-based passive radar. IEEE J Sel Top Appl Earth Obs Remote Sens, 14: 1184-1193. https://doi.org/10.1109/JSTARS.2020.3037200

He Z, Yang Y, Chen W, Weng D (2022) Range resolution improvement of GNSS-based passive radar via incremental Wiener filter. IEEE Geosci Remote Sens Lett, 19: 1-5. https://doi.org/10.1109/LGRS.2021.3130062

559 Hu Y, Yuan X, Liu W, Hu Q, Wickert J, Jiang Z (2022) An SVM-Based Snow Detection
560 Algorithm for GNSS-R Snow Depth Retrievals. IEEE J Sel Top Appl Earth Obs
561 Remote Sens, 15: 6046-6052. https://doi.org/10.1109/JSTARS.2022.3193113

562 Li Z, Santi F, Pastina D, Lombardo P (2017) Multi-Frame Fractional Fourier Transform
563 Technique for Moving Target Detection with Space-Based Passive Radar. IET
564 Radar Sonar Navig, 11(5): 822-828. https://doi.org/10.1049/iet-
565 rsn.2016.0432

566 Lu Y, Yang D, Li W, Ding J, Li, Z (2013) Study on the New Methods of Ship Object
567 Detection Based on GNSS Reflection. Marine Geodesy, 36(1): 22-30.
568 https://doi.org/10.1080/01490419.2012.747456

569 Ma H, Antoniou M, Pastina D , Santi F, Pieralice F, Bucciarelli M, Cherniakov M (2018)
570 Maritime moving target indication using passive GNSS-based bistatic radar.
571 IEEE Trans Aerosp Electron Syst, 54(1): 115-130.
572 https://doi.org/10.1109/TAES.2017.2739900

573 Pastina D, Santi F, Pieralice F, Antoniou M, Cherniakov M (2021) Passive radar
574 imaging of ship targets with GNSS signals of opportunity. IEEE Trans Geosci
575 Remote, 59(3): 2627-2642. https://doi.org/10.1109/TGRS.2020.3005306

576 Richards A (2014) Fundamentals of Radar Signal Processing. New York, USA.

577 Santi F, Pastina D, Bucciarelli M (2017) Maritime Moving Target Detection Technique
578 for Passive Bistatic Radar with GNSS Transmitters. In: the 18th International
579 Radar Symposium (IRS), Prague, 28-30 June, pp 1-10.

580 Shi S, Liu J, Li T, Tian W (2017) Basic performance of space-surface bistatic SAR
581 using BeiDou satellites as transmitters of opportunity. GPS Solut, 21(2), 727-
582 737. https://doi.org/10.1007/s10291-016-0563-8

583 Simone D, Park H, Riccio D, Camps A (2017) Sea Target Detection Using Spaceborne
584 GNSS-R Delay-Doppler Maps: Theory and Experimental Proof of Concept
585 Using TDS-1 Data. IEEE J Sel Top Appl Earth Obs Remote Sens, 10(9): 4237-

4255. https://doi.org/10.1109/JSTARS.2017.2705350

Southwell J, Cheong W, Dempster G (2020) A Matched Filter for Spaceborne GNSS-R Based Sea-Target Detection. IEEE Trans Geosci Remote, 58(8): 5922-5931. https://doi.org/10.1109/TGRS.2020.2973142

Wang B, Cha H, Zhou Z, Tian B (2021) Clutter Cancellation and Long Time Integration for GNSS-Based Passive Bistatic Radar. Remote Sens, 13(4): 701-716. https://doi.org/10.3390/rs13040701

Wang Y, Li J, Chen J, Xu H, Sun B (2013) A parameter-adjusting polar format algorithm for extremely high squint SAR imaging. IEEE Trans Geosci Remote, 52(1): 640–650.

Zeng Z (2013) Passive bistatic SAR with GNSS transmitter and a stationary receiver. Dissertation, University of Birmingham

Zhou X, Wang P, Chen J, Men Z, Liu W, Zeng H (2022) A Modified Radon Fourier Transform for GNSS-Based Bistatic Radar Target Detection. IEEE Geosci Remote Sens Lett, 19: 1-5. https://doi.org/10.1109/LGRS.2020.3041623

Zuo R (2011) Bistatic synthetic aperture radar using GNSS as transmitters of opportunity. Dissertation, University of Birmingham

Author Biographies

Zhenyu He received his Ph.D. from the Hong Kong Polytechnic University, Hong Kong, China, in 2022. He is currently a lecturer in Hohai University, Nanjing, China. His research interests include GNSS-based passive radar for moving target detection and imaging.

Wu Chen is a professor in the Hong Kong Polytechnic University. Professor Chen has been actively working on GNSS related research for over 30 years. His main research interests are Geodesy and Geodynamics, Seamless positioning technologies, GNSS positioning and applications, system integration, GNSS performance evaluation, regional GPS network and SLA.

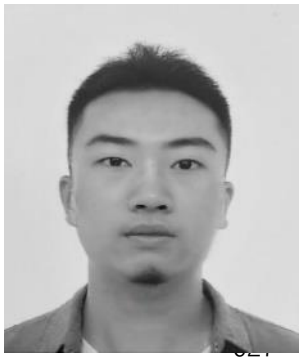

Yang Yang received a Ph.D. from the Hong Kong Polytechnic University, where he is a postdoctoral researcher. His research interests include GNSS software receivers, GNSS integrity monitoring, kinematic GPS, and sensor integration for various navigation systems.

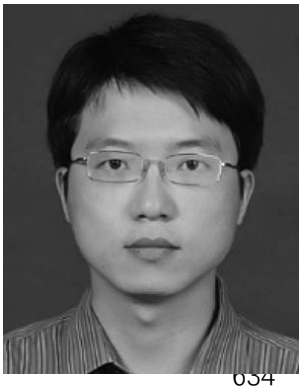

Mingwei Shen received a Ph.D. in the Nanjing University of Aeronautics and Astronautics, Nanjing, China, in 2008 and is a professor at HoHai University. His research interests include space-time adaptive processing (STAP) and SAR ground moving target indication (SAR/GMTI).